Proceedings World Geothermal Congress 2020+1
Reykjavik, Iceland, April - October 2021

Determination of Geothermal Anomalies Using Remote Sensing and Field Data in Paipa, Boyacá-Colombia

Rafael A. Calderón-Chaparro[1] and German Vargas-Cuervo[2]

[1]Dept. of Geoscience, [2]Dept. of Geography, National University of Colombia, Carrera 45 # 26-85, Bogotá D.C., Colombia

raacalderonch@unal.edu.co

Keywords: Remote Sensing, Thermal infrared, Landsat, Temperature, Paipa.

ABSTRACT

This research aims to integrate and interpret thermal infrared remote sensing data with geological and geophysical information of Paipa geothermal zone. Thermal bands of Landsat 7 ETM+ and Landsat 8 TIRS are used to retrieve the land surface temperature (LST). A radiometer station is used to record field data, like subsurface temperatures measured at one-meter depth, surface temperatures, air temperatures, relativity humidity, and atmospheric pressure. Two thermal Landsat images of different dates are corrected by emissivity and atmospheric distortions, using a single channel and split window algorithm to generate LST maps. One hundred ninety-seven points were used to generate a subsurface temperature map, finding six anomaly areas with temperature ranging from 19.1ºC to 37ºC. To validate the results of remote sensing a spatial comparison between land surface temperature anomalies and soil temperature anomalies were conducted; the results show a good spatial correlation between most anomalies of surface and subsurface temperature. Land surface temperature results indicate that thermal anomaly areas are correlated with porous sedimentary rocks at surface and faulted structures. Also, a comparison between low-resistivity zones and land surface temperature anomalies have an acceptable spatial correlation. Some of the LST anomaly areas are validated by field geothermal manifestations and geophysical results (low-resistivity zones). In conclusion, thermal infrared remote sensing data is a valuable tool for geothermal exploration areas, combined with field data and geological-geophysical information facilitate the detection of geothermal resources.

1. INTRODUCTION

In Colombia, the supply of energy is dominated by hydraulic (70.08%) and fossil power plants (27.22%) (DNP, 2017). Unlike other Latin American nations (i.e., Mexico, El Salvador, Chile), Colombia does not take advantage of its renewable energy resources. One of this renewable resource is geothermal energy that refers to the heat produced inside the earth. This energy is transported to the surface through water or steam (DiPippo, 2015), and is considered one of the cleanest energy on the planet (Dickson & Fanelli, 2003). The most important application of geothermal energy is electricity production; however, it also has several applications like heating and cooling spaces, baths, chemical production, among others (Lund & Boyd, 2015). According to Battocletti (1999), Colombia has a geothermal potential of 2,210 MW, which principally belongs to volcanic areas. Paipa is one prospective geothermal site located in the eastern cordillera; it is~130 km^2 in area and has occurrences of hot springs and steam vents. The area is characterized by rugged topography that difficult conventional geological and geophysical surveys. Despite, different field studies have been carried out in Paipa (Alfaro Valero C., 2002; Vásquez L., 2002; Velandia F., 2003; Cepeda & Pardo, 2004; Alfaro Valero & Espinoza, 2004; Alfaro Valero C. 2005; Alfaro Valero C., 2005b; Ortiz & Alfaro, 2010; Franco J., 2012; Vásquez L., 2012; Rodríguez Rodríguez & Vallejo Rodríguez, 2013; Llanos et al., 2015; Moyano I., 2015; Rueda J., 2016). Currently, there have been no studies using satellite thermal infrared (TIR). Thermal remote sensing is an alternative and complement for surveys in Paipa geothermal area.

Thermal remote sensing has become a useful tool for the exploration of geothermal resources. Its attractive is the quick mapping of thermal anomalies and the temperature quantification of these. TIR technology can perceive minor temperature anomalies on the order of 0.05–0.5°C over areas of up to hundreds of square kilometers (Darge et al., 2019). During the last 50 years, the use of this technology has helped to identify surficial temperature anomalies related to volcanic and higher anomaly heat flow areas (Allis et al., 1999; Ayenew, 2001; Haselwimmer et al., 2013). Multispectral satellites, such as Landsat 7 ETM+ and Landsat 8 OLI/TIRS have thermal bands that are used to determine thermal anomalies in volcanic and geothermal areas (Mia et al., 2014, Chan & Chang, 2018, Cesarian et al., 2018; Sekertekin & Arslan, 2019). Landsat 7 ETM+ has a thermal band with a spatial resolution of 60 m and a spectral range between 10.4 and 12.5 µm. A single-channel algorithm was applied to this band to determine surface temperature anomalies (Jiménez-Muñoz et al., 2009). Similarly, Landsat 8 TIRS has two thermal bands with a spatial resolution of 100 m and a spectral range between 10.6 to 11.19 µm (band 10) and 11.5 to 12.51 µm (band 11). A two-channel algorithm (Split Window) was applied to these two bands (Du et al., 2015). Although TIR technology is effective, it is advisable to record soil temperature measurements to validate the results of the thermal remote sensing.

Using this approach, this study used for the first time thermal remote sensing in the exploration of Paipa geothermal zone. We intend to demonstrate the effectiveness of the TIR technology to determine geothermal anomalies, supported by field measurements that allow the validation of satellite data. The main objective of this research is to define geothermal targets for commercial use (electricity, baths, greenhouses).

2. STUDY AREA

Paipa is located in the eastern Cordillera of Colombia. This region has an altitude between 2500 and 2800 m.a.s.l. The area is framed in the coordinatesW73º9'45.89'', N5º46'15.676'' and W73º3'16.069'', N5º38'42.717'' (Figure 1). The geology of the area includes rocks such as sandstones (K1u, K2lt, E1-2b, N1t, Qal), limestones (K1t), mudstones (K2ch, K2c, K2p, K2E1g), siltstones (K2pl), rhyolites, and volcanic deposits (Velandia, 2003) (Figure 2). The volcanic deposits are classified as ash flows, and ash falls, ignimbrites, and domes blocks; the rhyolites correspond to body domes (Cepeda & Pardo, 2004). Volcanism is associated with magmatic rise due to molten mantle material, perhaps due to the subduction of the Caribbean plate under South America (Jaramillo

& Rojas, 2003). According to the results of apatite fission tracks and U-Pb dating, the volcanic activity occurred between 5.9 and 1.8 Myr (Bernet et al., 2016). These age match with the maximum uplift time of the eastern cordillera. From geological, geochemical, and geophysical surveys carried out in Paipa propose the existence of two potential geothermal reservoirs, one deep with a temperature of~230ºC and another shallow with a temperature of~75ºC (Alfaro et al., 2017). The surface manifestations of the geothermal activity are indicated by several hot springs and one steam vent, and they are located around of Paipa Tourism Institute and El Delfín and La Playa pools.

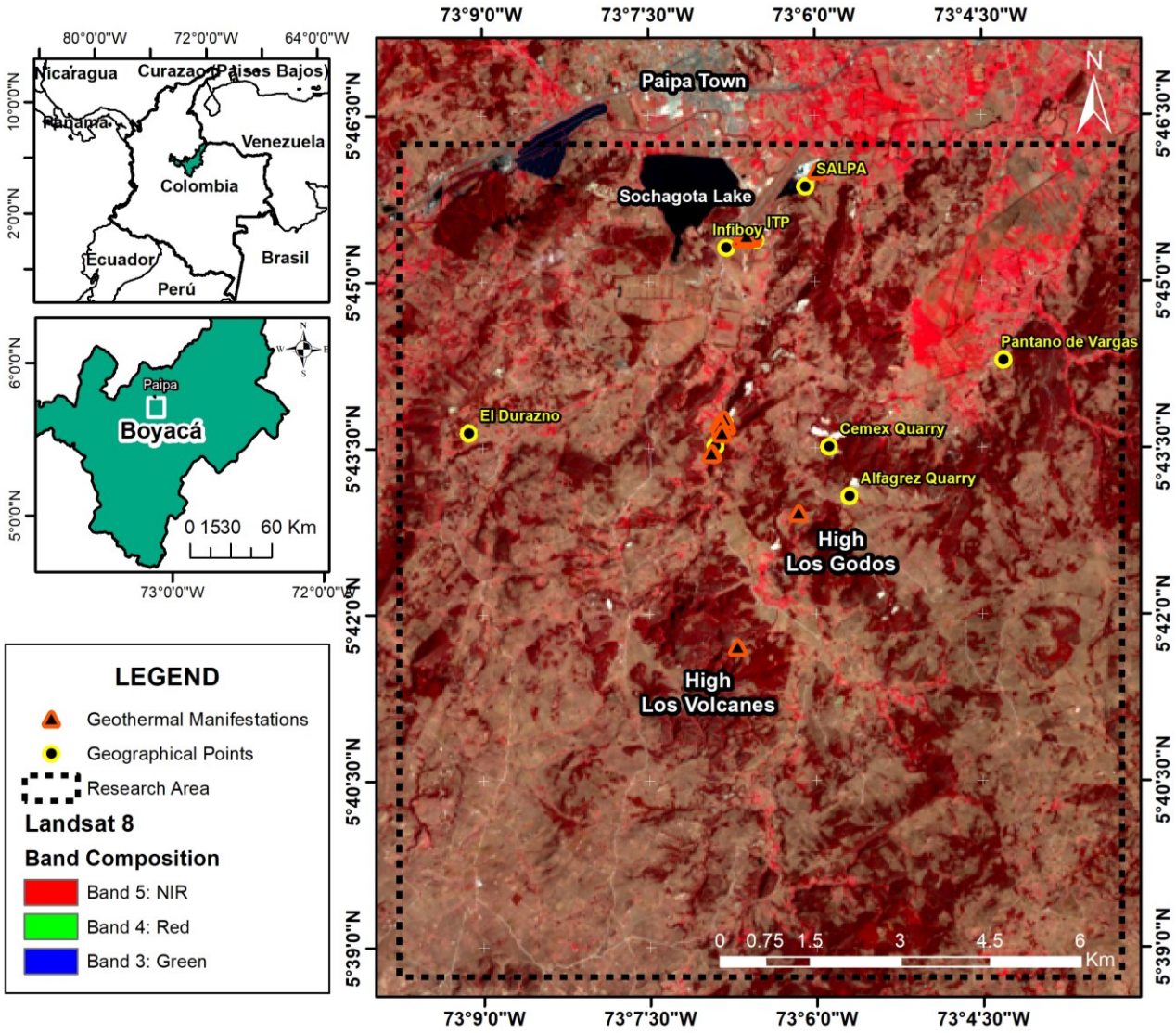

Figure 1. Location of the study area in Paipa-Boyacá, Colombia (the black dashed rectangle marks research area). The red edge triangles represent main geothermal manifestations, and yellow edge circles represent well know geographic reference points.

3. MATERIAL AND METHODS

3.1. Materials

3.1.1. Satellite data

Landsat images are primary information sources in this study. The images include scenes from Landsat 7 ETM+, Landsat 8 OLI/TIRS, MODIS/Terra and ALOS-PALSAR. The spectral bands of red (30m / pixel), near infrared (30m/ pixel) and thermal infrared (60m-100m/pixel) of Landsat images were used to determine the land surface temperature anomalies. We also used images of water vapor content of the product MOD05_L2 (1000m/pixel) of MODIS/ Terra, which is used to correct the thermal emissivity of the surface atmospherically. Also, a digital elevation model-DEM (12.5m/pixel) of the zone was obtained from the ALOS-PALSAR satellite.

The images cover path 7 and row 56 of Landsat images. Two Landsat diurnal images were used. These were acquired on the dates 2002-03-06 and 2016-02-01, for Landsat 7 and Landsat 8, respectively. These images were selected because they presented 0% cloudiness for the research area and are of excellent quality.

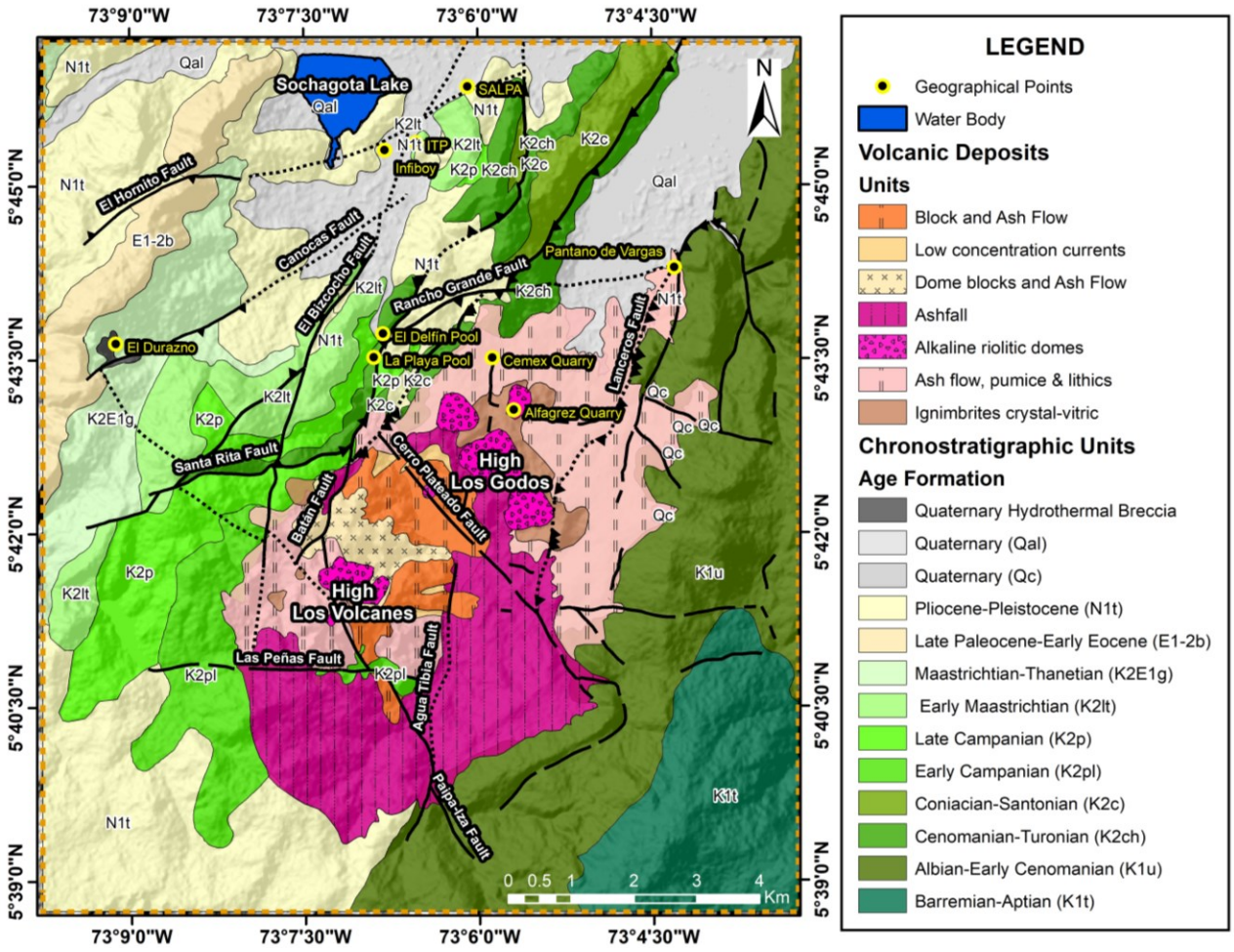

Figure 2. Geologic Map of the study area, from Velandia (2003) and Cepeda & Pardo (2004).

3.1.2. Field data

Fifty field measurements of soil, air, and surface temperatures, relative humidity, and atmospheric pressure were acquired. A radiometric station RS (powered by solar energy) and a FLIR CAT-S60 thermal camera were used. The RS is composed of a data logger, a solar panel, a radiometer, an infrared radiometer, a thermistor, and a multiparameter environmental sensor (Figure 3). Table 1 provides details of the RS sensors. Air and surface temperature data were used to correct and validate the temperature values of the satellite images. The soil temperature data was used to create a map of soil temperature anomalies in the area.

Figure 3. Radiometric Station (RS) used in field acquisition.

Table 1. Instruments used in the field data collection

Variable	Units	Sensor	Brand / Model
Soil Temperature	°C	Thermistor	Apogee / ST100
Surficial Temperature	°C	Non-contact Infrared thermometer	Apogee / SI-4H1
Object surficial Temperature	°C	Thermal camera	CAT FLIR / S60
Air Temperature	°C	VP-4	Decagon/PASS RHT
Vapor pressure	kPa		
Relative Humidity	%		
Atmospheric Pressure	kPa		

3.2. Methodology

This study was carried out with primary and secondary information (Figure 4). Primary information is satellite and field data. Secondary information, they are previous work as geological map (Velandia, 2003), soil temperature data (Rodríguez & Vallejo, 2013), magnetotelluric survey (González-Idárraga et al., 2017), and geothermal information (Alfaro et al., 2017). First, the satellite images were processed digitally; second, a soil temperature map was generated; third, primary and secondary information were overlayed; finally, geothermal anomalies were interpreted.

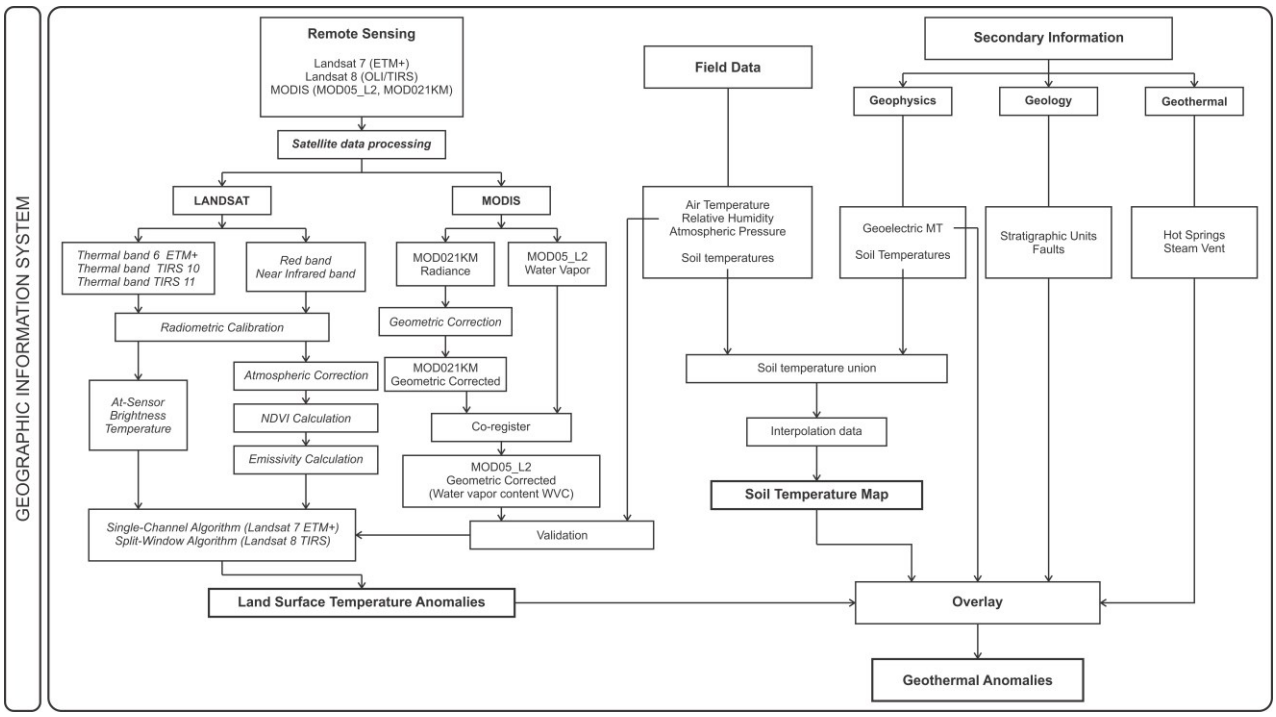

Figure 4. General Methodological Framework.

3.3. Data processing

3.3.1. Satellite data processing

The physical basis of LST retrieval is the Blackbody radiation and the Planck function. Using this approach, different authors have proposed algorithms to retrieve LST. In this study, we used a single channel algorithm for Landsat 7 ETM+ (Jiménez-Muñoz & Sobrino, 2003; Jiménez-Muñoz et al., 2009) and a split window algorithm for Landsat 8 TIRS (Du et al., 2015). Before using these algorithms, digital numbers of Landsat have to be radiometrically calibrated DN→L_λ (USGS, 2018 and 2016). Once with the radiance values (L_λ), an atmospheric correction was applied to the visible and near-infrared bands. This correction is applied due to absorption and dispersion processes, as a result of the existence of water vapor, gases (Ozone, Oxygen, Carbon Dioxide, Nitrogen Oxide, etcetera.) and molecules in the atmosphere, which affect the amount of radiation received by the sensor. The atmospheric correction module Fast Line-of-Sight Atmospheric Analysis of Spectral Hypercubes (FLAASH) was used. FLAASH is a first-principles atmospheric correction tool incorporating the MODTRAN (MODerate resolution atmospheric TRANsmission) radiation transfer model to compensate for atmospheric effects, which is being established by the Air Force Phillips Laboratory, Hanscom AFB and Spectral Sciences, Inc. (Adler-Golden et al., 1998 in Chan et al., 2018). Spectral reflectance of the visible (ρ_{red}) and near-infrared (ρ_{NIR}) bands were obtained. Next, thermal surface emissivity is calculated using NDVI threshold method ($NDVI^{TH}$). Sobrino et al., (2004) proposed this method, it is based on the determination of the emissivity for each pixel, based on the proportion of vegetation Pv, obtained from the values of the Normal Differential Vegetation Index (NDVI), equation (1).

$$NDVI = \left(\frac{\rho_{\text{NIR}} - \rho_{RED}}{\rho_{\text{NIR}} - \rho_{RED}} \right) \quad (1)$$

$NDVI^{TH}$ consider three different surface classes, dependent on the NDVI values: a) Bare soil (NDVI <0.2), b) mixed surface (0.2≥NDVI≤0.5), and c) Surface fully covered with vegetation (NDVI> 0.5).

a) Bare soil (NDVI <0.2): The emissivity value for Landsat 7 images is established as constant ε = 0.97. In the case of Landsat 8 images, the emissivity was determined from the ρ_{red}, for each of the thermal bands, ε_{10}=0.973-0.047$\rho_{red,}$ and ε_{11}=0.984-0.026ρ_{red} (Yu et al., 2014).
b) Mixed surface (0.2 ≥ NDVI ≤ 0.5): The pixels are considered as a mixture between vegetation and bare soil. The emissivity is obtained as a function of the proportion of vegetation, as follows, $\varepsilon=\varepsilon_v P_v+\varepsilon_s (1-P_v)+d\varepsilon$, where, ε_v is the emissivity of the vegetation, ε_s is the soil emissivity, and dε is a term which includes the effect of geometric distribution of natural surfaces and internal reflections (Sobrino et al., 2004). The P_v is calculated from the following equation, $P_v = \left[\frac{NDVI-NDVI_{min}}{NDVI_{max}-NDVI_{min}}\right]^2$, where $NDVI_{min}$=0.2 and $NDVI_{max}$=0.5. dε is calculated in the following way $d\varepsilon=(1-\varepsilon_s)(1-P_v)*F*\varepsilon_v$, where F is a form factor, with a mean value of 0.55, which considers different kinds of geometric distribution.

For the case of the Landsat 8 thermal bands, the average emissivity values of the soil and vegetation of each one were taken into account: ε_{s10}= 0.9668, ε_{s11}= 0.9747, ε_{v10}= 0.9863 y ε_{v11}= 0.9896 (Yu et al., 2014).

c) Surface fully covered with vegetation (NDVI> 0.5): It was assumed for both Landsat 7 and Landsat 8 images, a constant value ε = 0.99.

Finally, the LST result is computed from a single channel (Landsat 7) and split window (Landsat 8) algorithm, equations 2 and 3, respectively.

$$LST = \gamma\left[\frac{1}{\varepsilon}\left(\varphi_1 L_{sen} + \varphi_2\right) + \varphi_3\right] + \delta \quad (2)$$

Where ε is the emissivity of the surface; γ and δ are two parameters dependent on the Planck functions, expressed in the following way, $\gamma \approx \frac{T_{sen}^2}{b_\gamma L_{sen}}$ and $\delta \approx \frac{T_{sen}^2}{b_\gamma}$, where T_{sen} is the temperature of brightness at the sensor $T_{sen} = \frac{K_2}{ln\left(\frac{K_1}{L_\lambda}+1\right)}$, where K_1 [W.m^{-2}.sr^{-1}.μm^{-1}] and K_2 [K] are calibration constants (Table 2); Lλ is the spectral radiance in the sensor [W/(m2.sr.μm)] and ln is the natural logarithm. ; b_γ is a constant, with a value of 1277 K and L_{sen} is the spectral radiance at the sensor. Finally, φ_1, φ_2, φ_3 are atmospheric functions, $\varphi_1 = 0.14714\omega^2 - 0.15583\omega + 1.1234$; $\varphi_2 = -1.1836\omega^2 - 0.37607\omega - 0.52894$ and $\varphi_3 = -0.04554\omega^2 + 1.8719\omega - 0.39071$, where ω is the water vapor content (WVC) in the atmosphere in g/cm^2. The product MOD05_L2 of the MODIS sensor, offers continuous values of ω at a spatial resolution of 1 km^2, being appropriate due to the small spatial variation of ω in the atmosphere (Ren et al., 2015). The values of WVC of the product MOD05_L2 were validated using the values of relative humidity and air temperature, collected in the field, by applying next equation $WVC = 0.0981\left(10 * 0.6108 * exp\left[\frac{17.27*T_0}{237.3+T_0}\right] * RH\right) + 0.1697$, where T_0 is the surface air temperature, RH is the relative humidity of the air, and WVC is given in g/cm^2.

The WVC values obtained from the field data vary from 0.52 g/cm^2 to 1.46 g/cm^2, which are very similar to the average values of WVC obtained by the MODIS sensor in the time of the Landsat 7 image (Table 3). This similarity allowed the validation of the WVC satellite values.

Table 2. Calibrations constants used to convert spectral radiance in brightness temperature, for Landsat 7 ETM+ and Landsat 8 TIRS.

Satellite	Band	K_1	K_2
Landsat 7	6	666.09	1282.71
Landsat 8	10	774.8853	1321.0789
	11	480.8883	1201.1442

Table 3. Water vapor content statistics of the MOD05_L2 image acquired March 6, 2002.

Statistics	Water vapor content
Min	0.706861
Max	1.71515
Mean	1.145315

$$LST = b_0 + \left(b_1 + b_2\frac{1+\varepsilon}{\varepsilon} + b_3\frac{\Delta\varepsilon}{\varepsilon^2}\right)\frac{T_i + T_j}{2} + \left(b_4 + b_5\frac{1-\varepsilon}{\varepsilon} + b_6\frac{\Delta\varepsilon}{\varepsilon^2}\right)\frac{T_i + T_j}{2} + b_7\left(T_i + T_j\right) \quad (3)$$

Where T_i and T_j are the brightness temperatures of bands 10 and 11 of Landsat 8, respectively; ε is the average emissivity of the thermal bands $\varepsilon=(\varepsilon_i+\varepsilon_j)/2$; Δε is the difference of the emissivity $\Delta\varepsilon=\varepsilon_i-\varepsilon_j$, and b_0, b_1, ...b_7 are the coefficients determined for each WVC range. The coefficients used correspond to the values defined for a range of WVC between 0.0 and 2.5 g/cm^2, determined thanks to the record of the MODIS images and the field values, whose average value is 1.3 g/cm^2.

3.3.2. Field data processing

A soil temperature map of the Paipa geothermal system was made. One hundred ninety-seven temperature probes were used, recorded at depths greater than one meter. The Geostatistical wizard tool of ArcMap© was used by applying an interpolation method of kriging. The 197 soundings are constituted by 147 soundings taken by the CGS (Rodríguez & Vallejo, 2013) and 50 new temperature data acquired in the field throughout this study.

3. RESULTS AND DISCUSSION

3.1. Satellite image processing

Landsat bands were radiometrically calibrated and atmospherically corrected. The results were used to calculated NDVI, land surface emissivity, and thermal anomalies. NDVI values range between -1 and 1 for both images (2002-03-06 and 2016-02-01) (Figure 5a and 5b). Figure 5a and 5b could be considered land cover maps, the values above 0.5 represent vegetated areas, values between 0.2 and 0.5 represent mixed surfaces (bare soil and vegetation), values between 0.0 and 0.2 are bare soil and values below 0 represent water. It is readily appreciable that most of the land cover in both images is dominated by mixed surface (yellow area). The Mixed surface increased for 2016, almost wholly reducing the bare soil area observed in 2002. The vegetated area increased a little for 2016 but in general, occupies 40% of the study area. Different authors agree that dense vegetation masks the thermal emissivity of the soil, therefore, it is better to have bare soil and mixed surfaces, so the sensor can accurately record the thermal signal of the underground (Eneva et al., 2006; Kuenzer & Dech, 2013; Citra Aulian Chalik et al., 2019).

The land surface emissivity was calculated using the $NDVI^{TH}$ method; the values range between 0.97 and 0.99. Then the land surface temperature (LST) was estimated using a single channel and split-window algorithm for Landsat 7 and Landsat 8, respectively. LST in the study area varies from 20ºC to 50ºC for both thermal Landsat imagery (Figure 6a and 6b). Anomalous areas are produced by higher LST ranging from 43ºC to 50ºC. These anomalies have a temperature 3-8ºC higher than the surrounding background, and they could have a geothermal origin. Most temperature anomalies are located to the west of the study area.

3.2. Field data processing

Figure 7 shows the soil temperature map retrieve by the 197 temperature soundings in the study area. The lowest temperature around the area is 15ºC while the highest temperature is 37ºC. It is assumed that the temperatures over 19.1 ºC have geothermal influence. The temperature map shows six thermal anomalies numbered from 1 to 6, possibly associated with a geothermal genesis. Anomalies 1 and 4 are located where the two unique hydrothermal discharge zones of the geothermal system of Paipa come to the surface (hot springs of ITP-Infiboy and El Delfín-La Playa Thermal Pools).

3.3. Spatial correlation between LST anomalies and soil temperature anomalies, surficial geothermal manifestations, resistivity profiles, and geology

3.3.1. LST and Soil temperature anomalies

Surface temperature anomalies can be used with confidence once they have been appropriately validated. The approach used here is the spatial comparison between surface temperature anomalies and soil temperature anomalies since the latter is a direct expression of the heat present in the underground. In general, five of the six soil temperature anomalies correspond spatially with satellite surface temperature anomalies (Figure 8 a to 1), demonstrating the geothermal component in thermal satellite images.

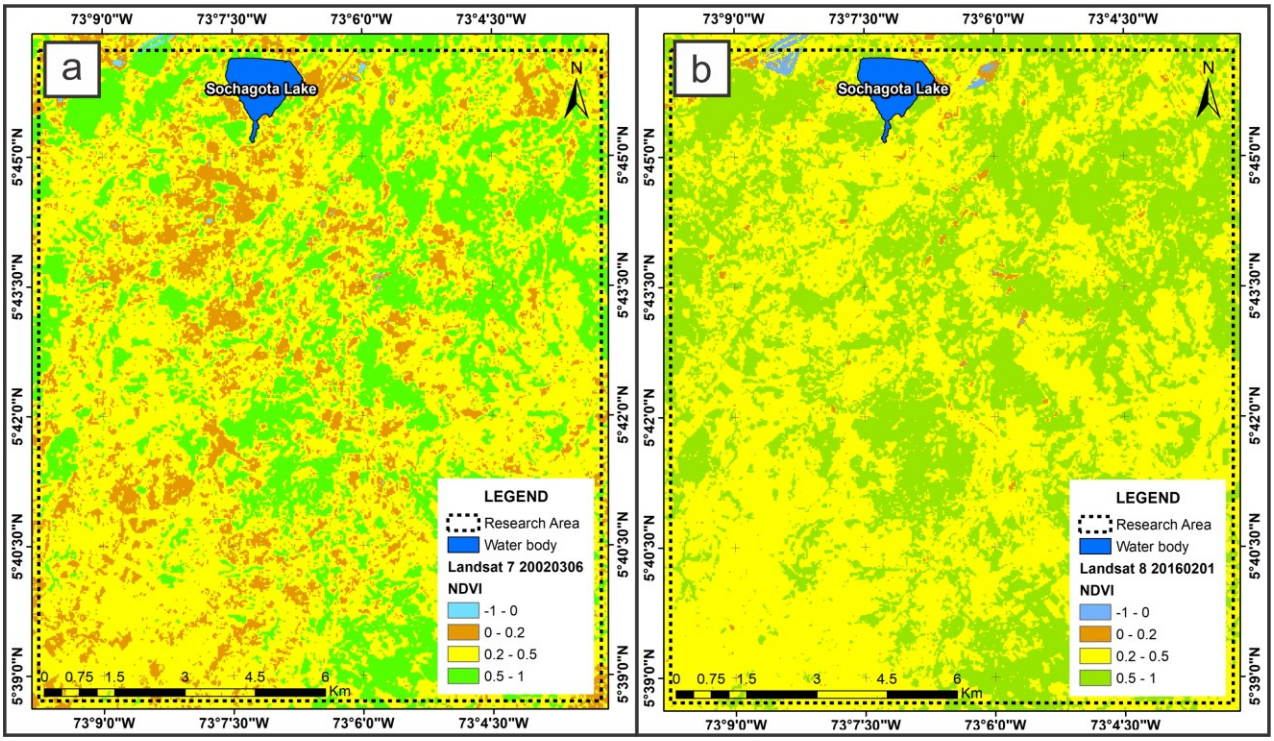

Figure 5. NDVI maps. a) Landsat 7 ETM+, March 06, 2002. b) Landsat 8 OLI, February 01, 2016.

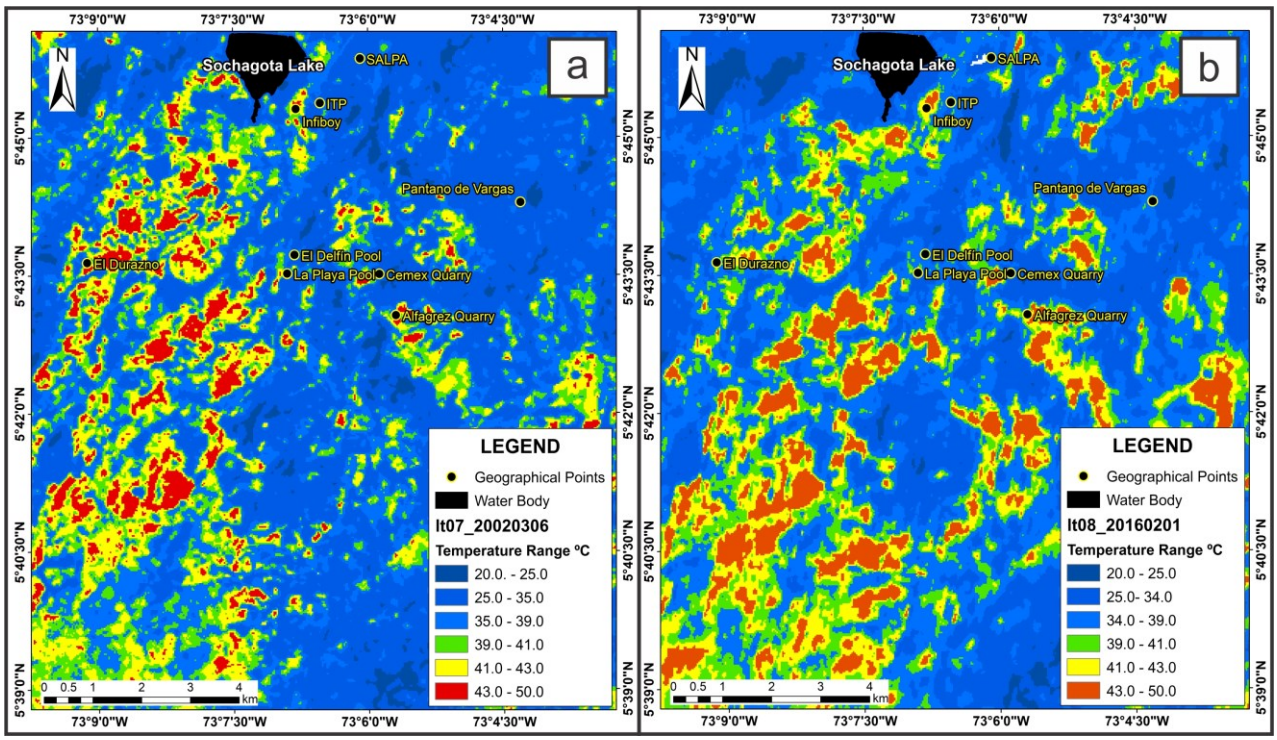

Figure 6. LST maps. a) Landsat 7 ETM+, March 06, 2002. b) Landsat 8 OLI, February 01, 2016.

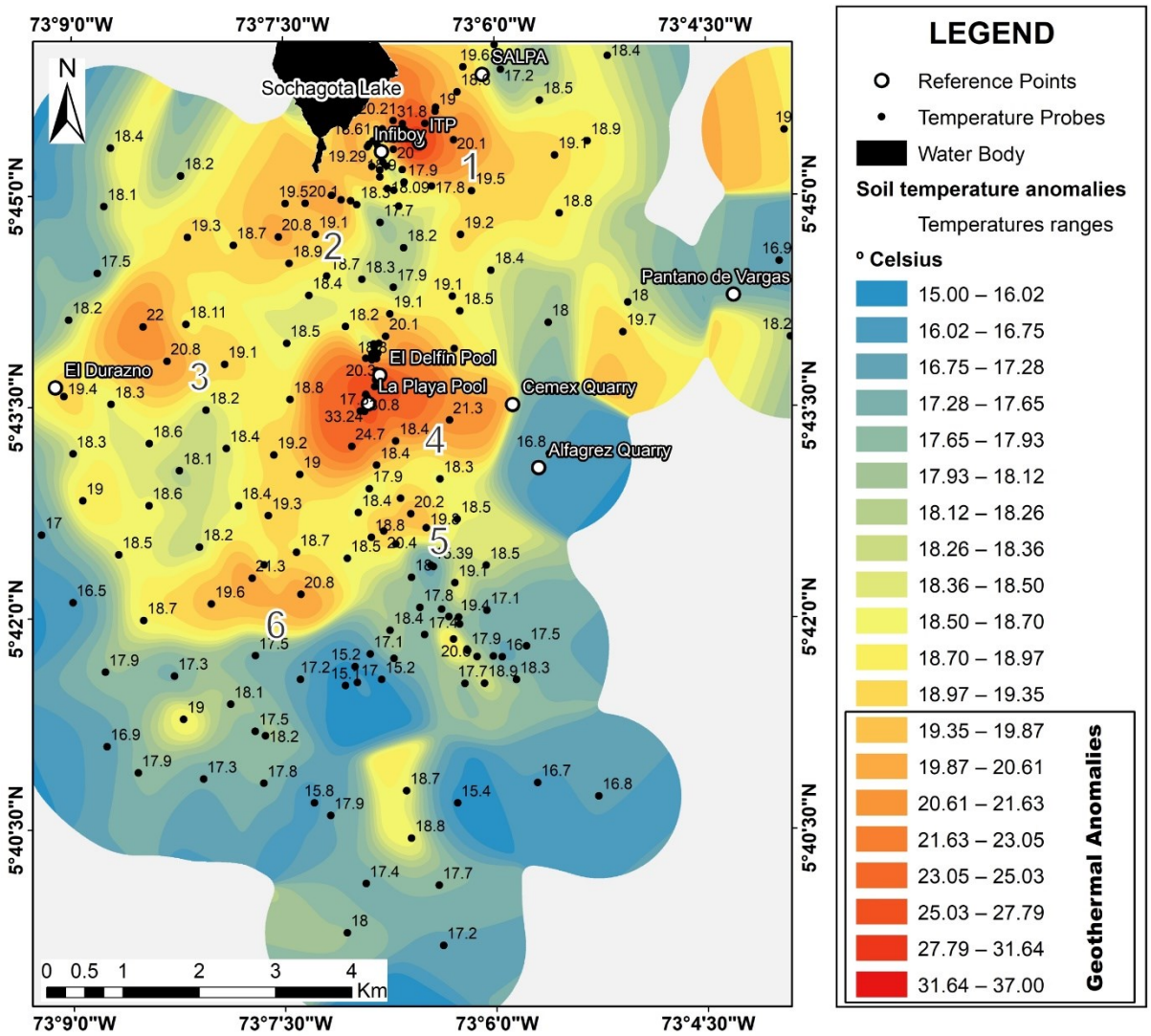

Figure 7. Soil temperature map of the study area.

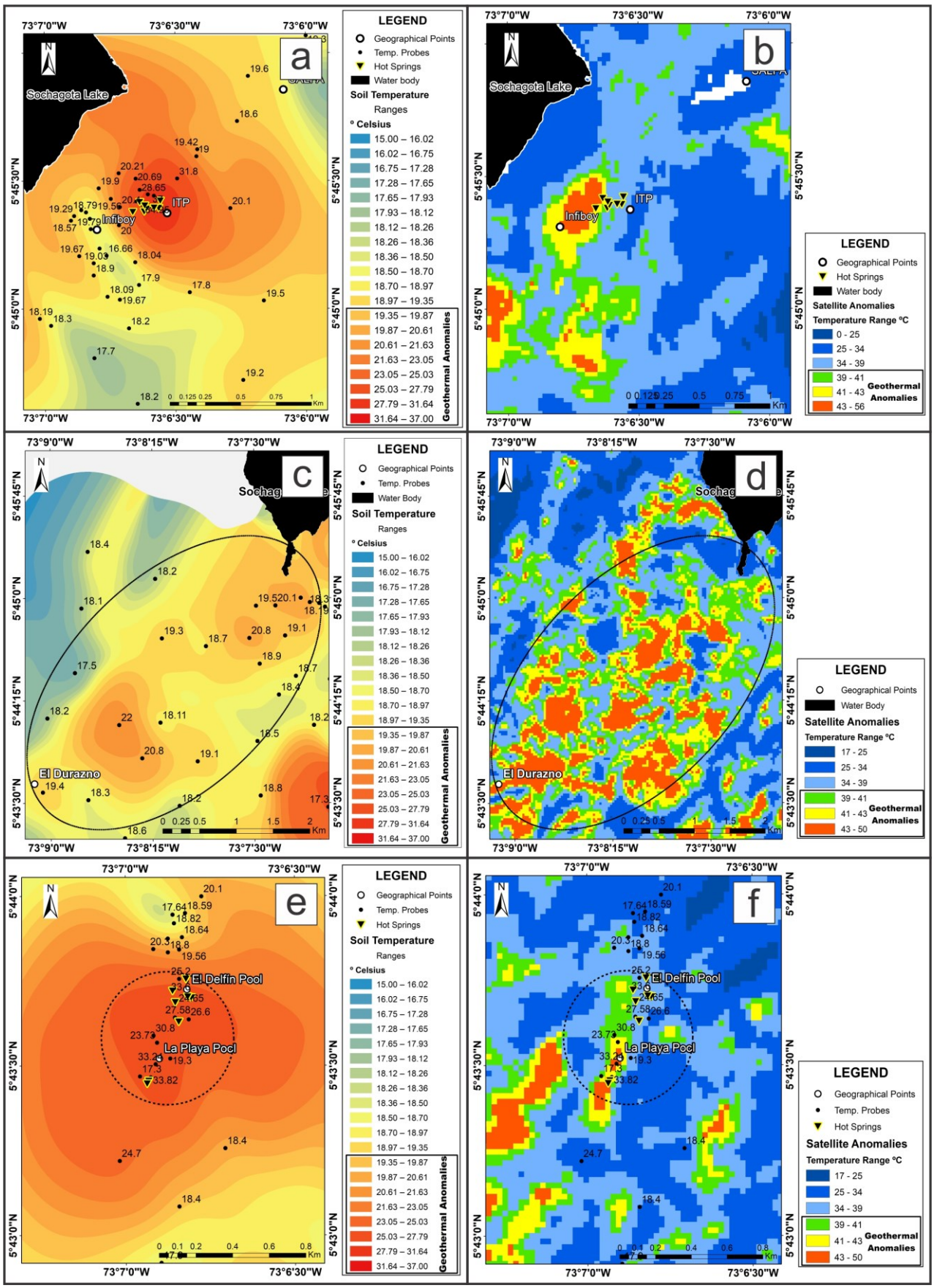

Figure 8. Spatial comparison of soil temperature anomalies and satellite temperature anomalies. a-b) Anomalies to the southeast of Lake Sochagota; c-d) Anomalies to the southwest of Lake Sochagota towards the Durazno sector; e-f) Anomalies to the sector of El Delfín and La Playa pools, where the presence of the second most important manifestations of the Paipa geothermal system occurs.

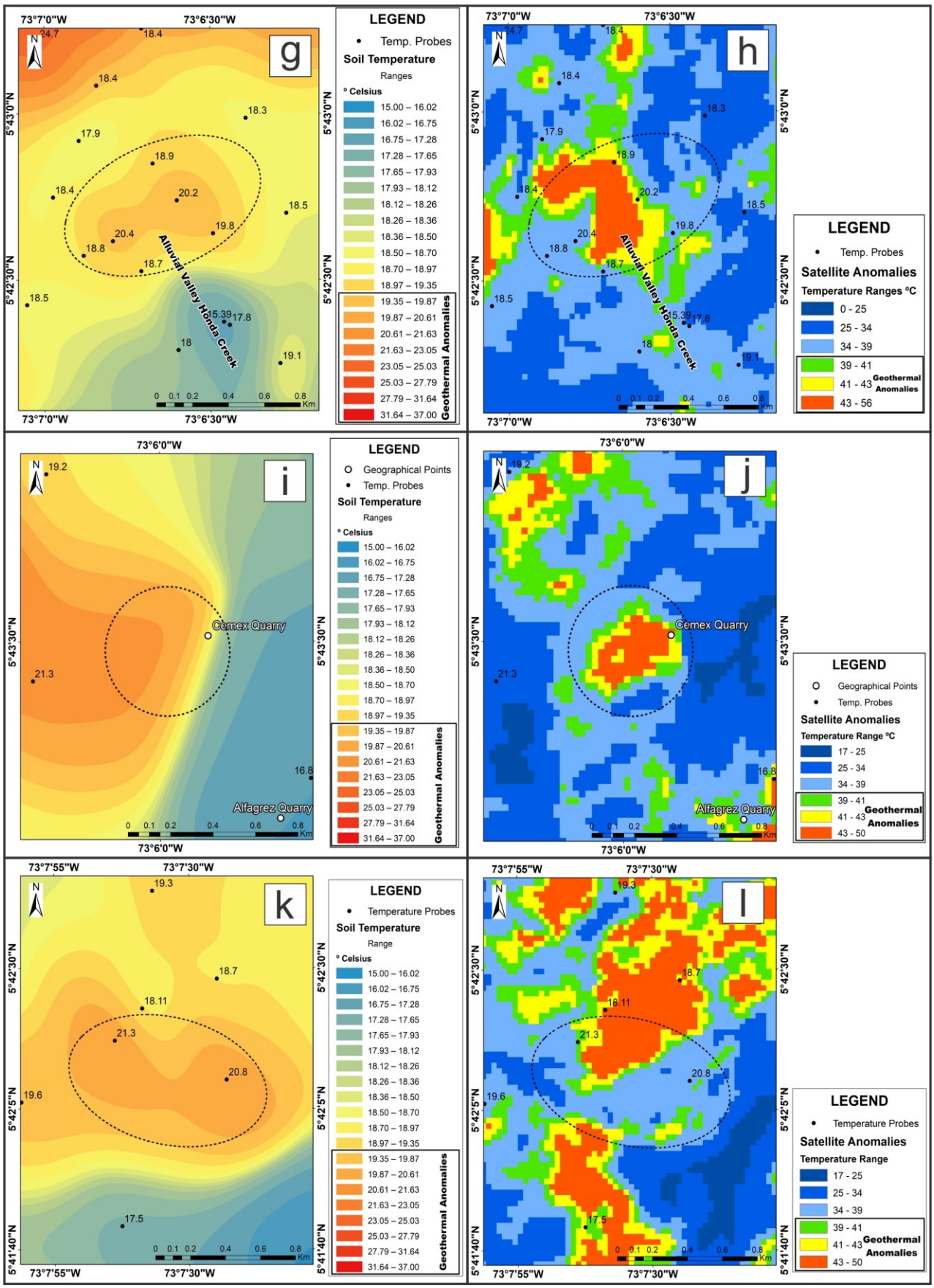

Continuation figure 8. Spatial comparison of soil temperature anomalies and satellite temperature anomalies. g-h) Anomalies to the southeast of the El Delfín and La Playa pools, on the alluvial valley of the Honda creek; i-j) Anomalies to the east of the El Delfín and La Playa pools, close to Cemex quarry; k-l) Anomalies to the southwest of the El Delfín and La Playa pools, and northwest of Los Volcanes high.

3.3.2. LST and Surficial geothermal manifestations

In the Paipa geothermal zone exist two hydrothermal discharge zones, one southeast of Sochagota lake (ITP-Infiboy hot springs) and the second 3.5 km to the south of the same lake (El Delfín-La Playa hot springs). In the ITP-Infiboy area, there are ten hot springs, and in the El Delfín-La Playa area, there are eight hot springs and one steam vent (Alfaro et al., 2017). The temperature of the spring water at ITP-Infiboy is as high as 72.1ºC (Figure 9c), and at El Delfín-La Playa is as high as 54.1ºC (Figure 10b). These surficial geothermal manifestations validate two of the thermal anomalies. Figures 9a and 10a show the correlation between the hot springs and the thermal anomalies retrieve by the Landsat 7 thermal image.

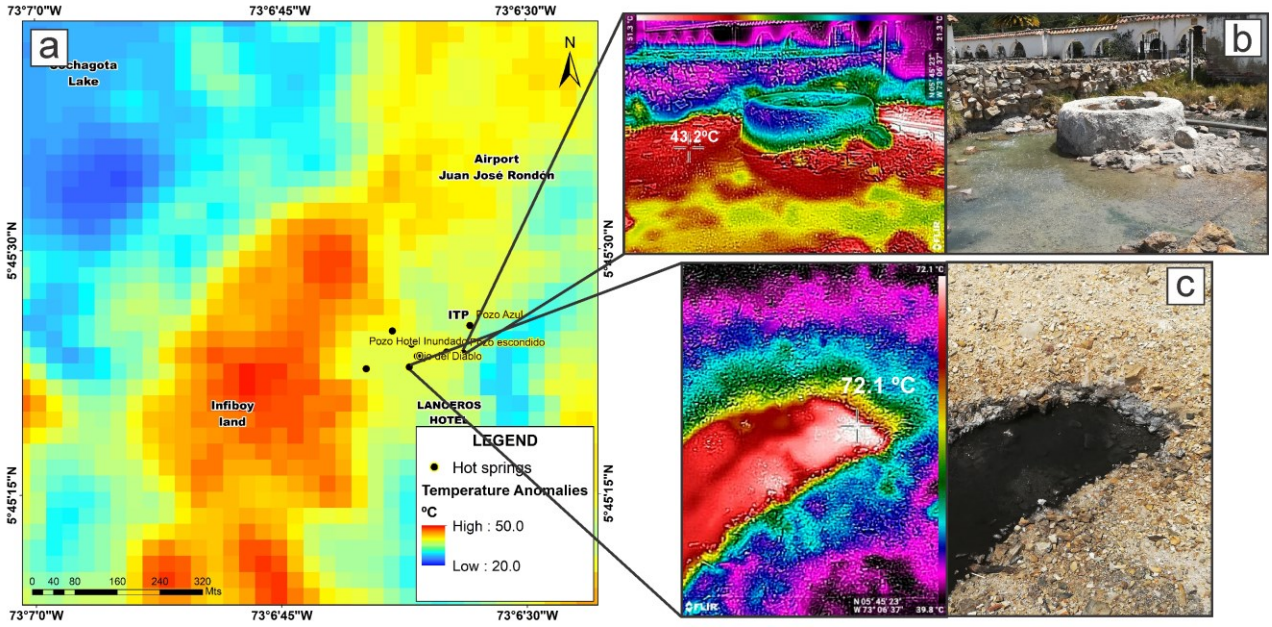

Figure 9. a) Overlaying hot springs and thermal anomalies Landsat 7. b) Thermal and visible photography of the Hot spring located next to the Hotel Lanceros; a maximum temperature of 51.3°C was recorded. c) Thermal and visible picture from the hot spring of the devil's eye; a temperature of 72.1°C was registered.

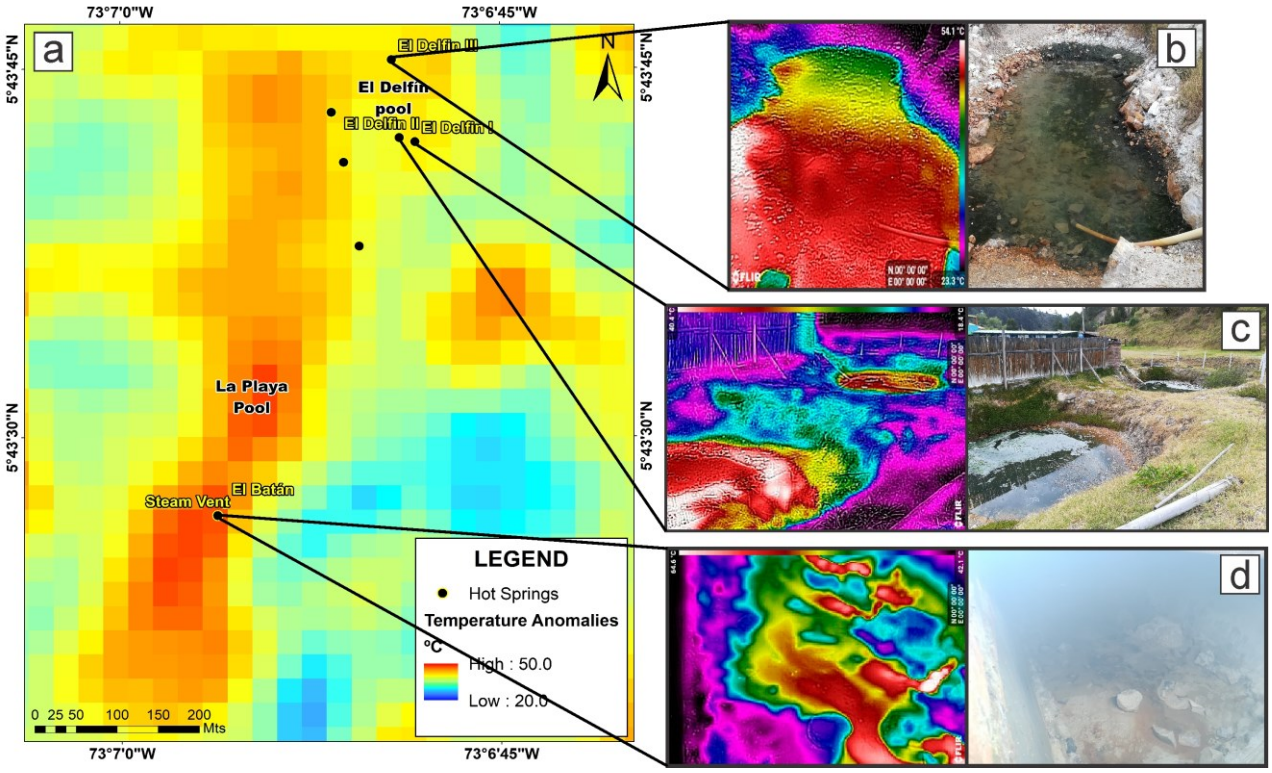

Figure 10. a) Overlaying hot springs and thermal anomalies Landsat 7. b) Thermal and visible picture of the spring III El Delfín, it has a temperature of 54.1°C. c) Thermal and visible picture of hot springs I and II El Delfín. d) Thermal and visible picture of the steam vent in the La Playa sector; a maximum temperature of 64.6°C was registered.

3.3.3. LST and Resistivity profiles

Magnetotelluric (MT) survey is applied for exploring structures of the geothermal reservoir (Chan et al., 2018). MT is an electromagnetic method in the frequency domain that obtain the underground resistivity after the electric and magnetic fields are calculated (Vozoff (1972) in González-Idárraga et al., 2017). One hundred sixty-two MT soundings were acquired for the Paipa geothermal area. Thus six 2D resistivity profiles were obtained (González-Idárraga et al., 2017). Figure 11 shows the location of the six 2D resistivity sections. In the resistivity sections, the conductive anomalies (red) are associated with geothermal fluids. Figures 12-13-14-15 show the resistivity sections and their corresponding LST profiles; these profiles are inside the study area (dashed black line figure 11). Several low-resistivity anomalies observed in the resistivity sections are aligned with the high-temperature zones of the LST profiles.

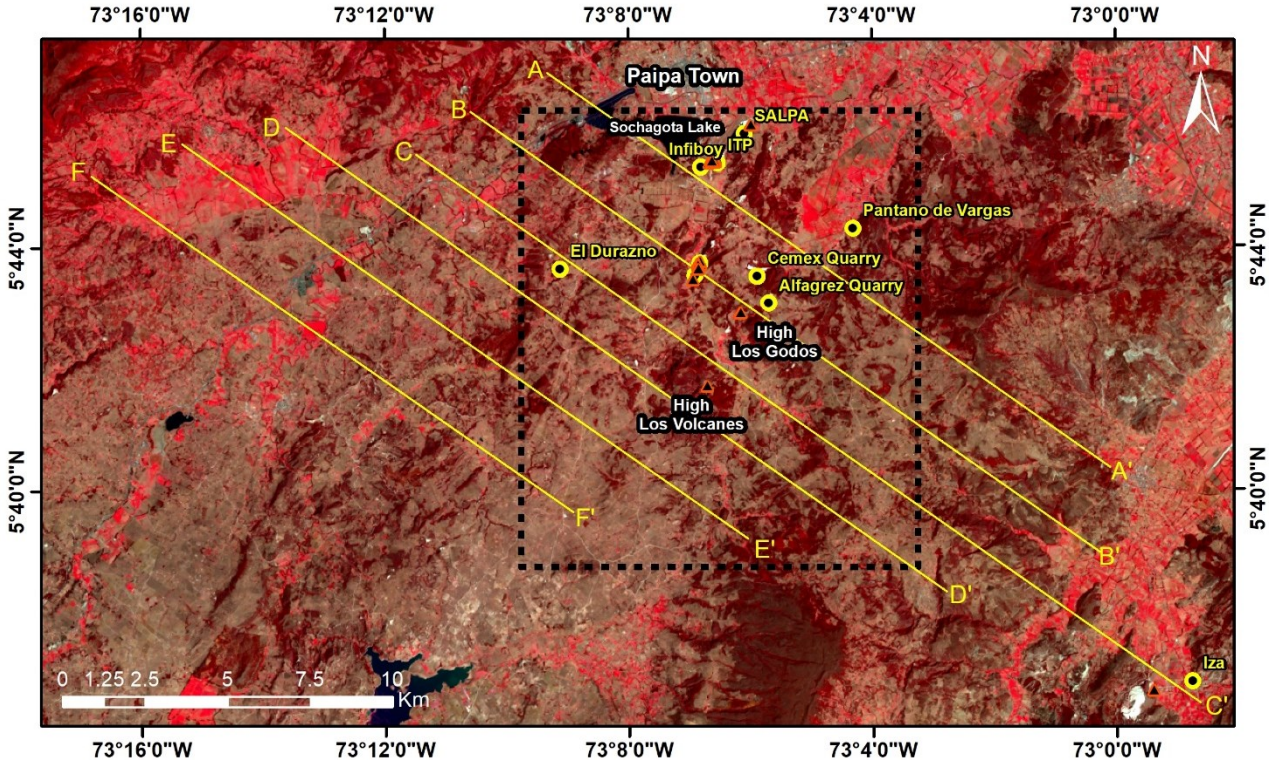

Figure 11. Location of the Magnetotelluric profiles (A-A', B-B', C-C', D-D', E-E', F-F'). The dashed black line is the study area ~130 km².

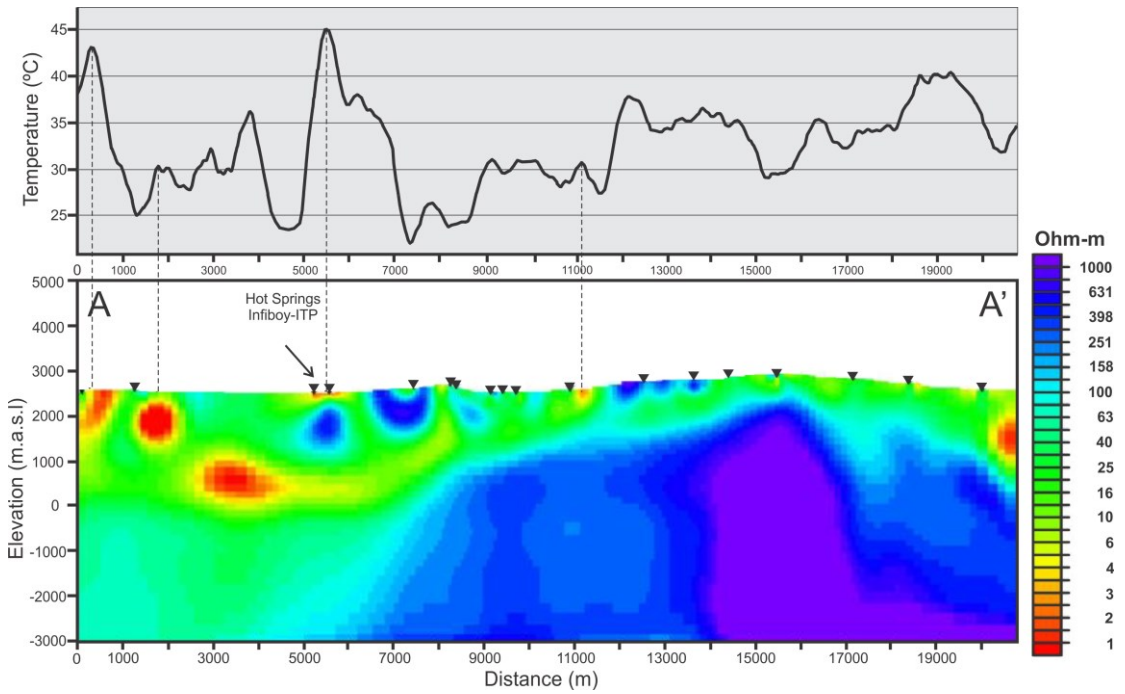

Figure 12. LST profiles compared with MT resistivity section of profile A-A' (González-Idárraga et al., 2017). The highest temperatures are located above conductivity anomalies.

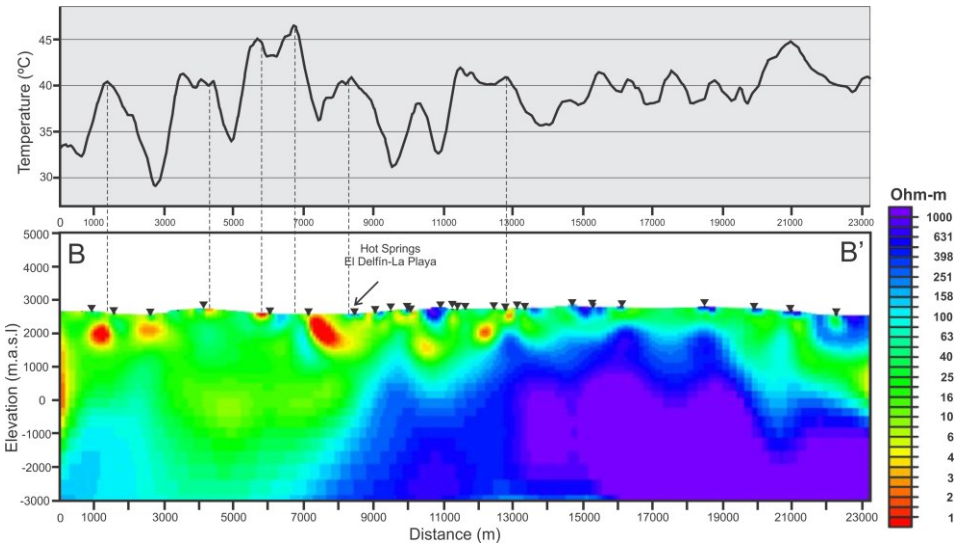

Figure 13. LST profiles compared with MT resistivity section of profile B-B' (González-Idárraga et al., 2017). Most of the highest temperatures are located above conductivity anomalies.

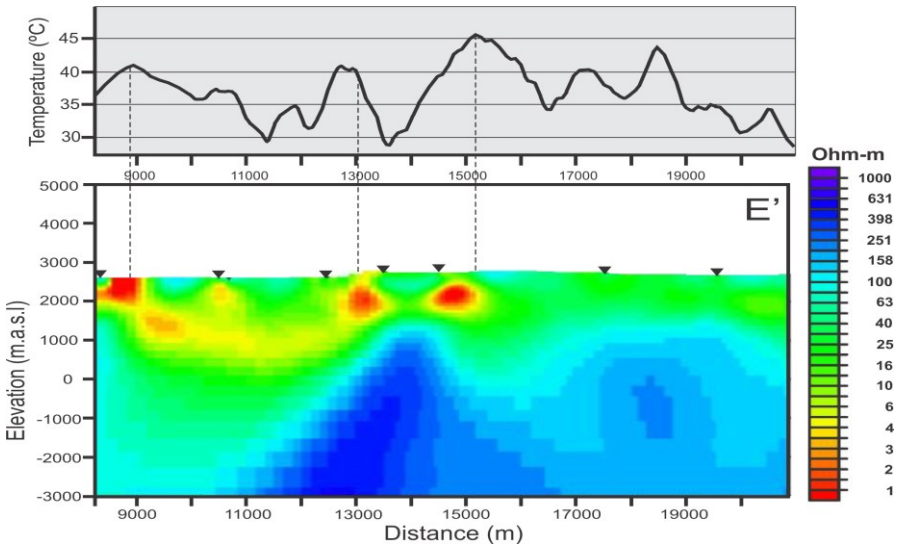

Figure 14. LST profiles compared with the final part of the MT resistivity section of profile E-E' (González-Idárraga et al., 2017). The highest temperatures are located above conductivity anomalies.

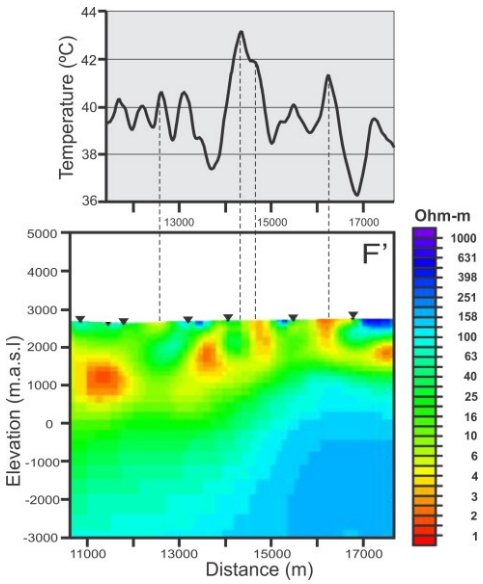

Figure 15. LST profiles compared with the final part of the MT resistivity section of profile F-F' (González-Idárraga et al., 2017). The highest temperatures are located above conductivity anomalies.

3.3.4. LST and Geology

Unlike geothermal reservoirs in active volcanic zones where thermal anomalies are located following a linear pattern according to the fault lineaments (Wu et al., 2012, Norini et al., 2015), the geothermal system of Paipa is different as the geothermal reservoirs are located through sedimentary rocks, which generates a lateral distribution of the hot fluids. The location of the thermal anomalies is found mainly to the northwest of the geothermal area (Figure 6). This location can be a product of the circulation of hot fluids at shallow depth, through porous stratigraphic units of the Tilatá N_1t, Bogotá $E_{1\text{-}2}b$, Guaduas K_2E_1g, Labor-Tierna K_2lt, and Los Pinos K_2p formations, and facilitated by the faults, which function as migration paths. Figure 2 shows the El Batán overthrust fault, with a northeast strike, of vergence towards the east, functioning as a limit (restricting), for the lateral circulation of hot fluids. The anomalies of surface temperatures found between the El Hornito and Canocas faults, southwest of Lake Sochagota (Figures 2 and 6), would be validated, according to the conceptual geothermal model proposed by the CGS (Alfaro et al., 2017), who proposed the existence of a secondary thermal system differing from the main one. This secondary system has a circulation of hot fluids at a shallow depth towards the northeast, by the porous sediments of the Guaduas K_2E_1g and Bogotá $E_{1\text{-}2}b$ formations.

4. CONCLUSIONS

The combination of TIR technology, field data, and previous works is useful to identify geothermal areas. The land surface temperature has been retrieved from the calibrated Landsat 7 ETM+ and Landsat 8 OLI/TIRS data. The land surface temperature anomalies were verified by comparison with the soil temperature anomalies, surficial geothermal manifestations, resistivity profiles, and geology. Several thermal anomaly areas were identified with the Landsat images; in general, the anomalies are located to the west of the study area, with a temperature 3-8ºC higher than their surrounding background. Two of these thermal anomalies are in close agreement with the geothermal manifestations (hot springs ITP-Infiboy and El Delfín-La Playa). On the other hand, five of six soil temperature anomalies have an acceptable correlation with the satellite thermal anomalies. Likewise, most of the conductivity anomalies are in close agreement with the highest temperature of the LST profiles. As a final point, the spatial distribution of the thermal anomalies allows interpreting that the hydrothermal fluids are accumulated through porous rocks and laterally control by the faults. In conclusion, the use of thermal satellite images for the correct identification of geothermal anomalies requires the incorporation of geological-geophysical analysis; this integration considerably improves the interpretation of satellite thermal data. It is essential to keep in mind that satellite thermal data is limited to detecting the surficial and shallow geothermal resources.

REFERENCES

Alfaro Valero, C. M. (2005). *Alteración hidrotermal en el sistema geotérmico de Paipa.* Servicio Geológico Colombiano. Bogotá: SGC.

Alfaro Valero, C. M., & Espinoza, O. (2004). *Sondeo preliminar de radón en el área geotérmica de Paipa.* Servicio Geológico Colombiano. Bogotá: SGC.

Alfaro Valero, C. M., Matiz León, J. C., Rueda Gutiérrez, J. B., Rodríguez Rodríguez, G. F., Gonzáles Idárraga, C. E., Beltrán Luque, M. Á., . . . Malo Lázaro, J. E. (2017). *Actualización del Modelo Conceptual del Área Geotérmica de Paipa.* Bogotá: Servicio Geológico Colombia.

Alfaro, C. (2002). *Estudio Isotópico de Aguas del Área Geotérmica de Paipa.* Bogotá: SGC.

Alfaro, C. (2005). *Modelo Conceptual Preliminar del Sistema Geotérmico de Paipa.* Bogotá: SGC.

Allis, R. G., Nash, G. D., & Johnson, S. D. (1999). Conversion of Thermal Infrared Surveys to Heat Flow: Comparisons from Dixie Valley, Nevada, and Wairakei, New Zealand. *Geothermal Resources Council, 23*, 499-504.

Ayenew, T. (2001). Surface Kinetic Temperature Mapping Using Satellite Spectral Data in Central Main Ethiopian Rift and Adjacent Highlands. *Ethiopian Journal of Science, 24*, 51-68.

Battocletti, L. (1999). *Geothermal resources in Latin America and the Caribbean.* BoB Lawrence & Associates. Retrieved from http://bl-a.com/ecb/PDFFiles/GeoResLAC.pdf

Bernet, M., Ureña, C., Amaya, S., & Peña, M. (2016). New thermo and geochronological constraints on the Pliocene-Pleistocene eruption history of the Paipa-Iza volcanic complex, Eastern Cordillera, Colombia. *Journal of Volcanology and Geothermal Research*, 299-309. doi:10.1016

Cepeda, H., & Pardo, N. (2004). *Vulcanismo de Paipa.* Bogotá D.C: Ingeominas.

Cesarian, D. P., Abir, I. A., & Isa, M. (2018). Comparison of In-Situ Temperature and Satellite Retrieved Temperature in Determining Geothermal Potential in Jaboi Field, Sabang. *Journal of Physics: Conference Series*. doi:doi:10.1088/1742-6596/1116/3/032008

Chalik, C. A., Saepuloh, A., & Suryantini. (2019). Detection of ground thermal anomaly under dense vegetation based on ASTER TIR images. (7. I. Workshop, Ed.) *IOP Conf. Series: Earth and Environmental Science*. doi:10.1088/1755-1315

Chan, H.-P., & Chang, C.-P. (2018). Exploring and monitoring geothermal and volcanic activity using Satellite Thermal Infrared data in TVG, Taiwan. *Terrestrial Atmospheric and Oceanic Sciences*, 387-404. doi:10.3319/TAO.2018.01.22.01

Chan, H.-P., Chang, C.-P., & Dao, P. D. (2018). Geothermal Anomaly Mapping Using Landsat ETM+ Data in Ilan Plain, Northeastern Taiwan. *Pure and Applied Geophysics*, 303-323.

Darge, Y. M., Hailu, B. T., Muluneh, A. A., & Kidane, T. (2019). Detection of geothermal anomalies using Landsat 8 TIRS data in Tulu Moye geothermal prospect, Main Ethiopian Rift. *International Journal Applied Earth Observation and Geoinformation*, 16-26.

Dickson, M. H., & Fanelli, M. (2003). *Geothermal Energy. Utilization and Technology.* Francia: UNESCO.

DiPippo, R. (2015). *Geothermal Power Plants: Principles, Applications, Case Studies and Environmental Impact* (Fourth ed.). North Dartmouth, Massachusetts, United States: Elsevier. Retrieved from https://www.sciencedirect.com/book/9780081008799/geothermal-power-plants

DNP. (2017). *Energy Supply Situation in Colombia.* Bogotá D.C: Departamento Nacional de Planeación.

Du, C., Ren, H., Qin, Q., Meng, J., & Zhao, S. (2015). A Practical Split-Window Algorithm for Estimating Land Surface Temperature from Landsat 8 Data. *Remote Sensing*, 647-665.

Eneva, M., Coolbaugh, M., & Combs, J. (2006). Application of Satellite Thermal Infrared Imagery to Geothermal Exploration in East Central California. *GRC Transactions*, 407-411.

Franco, J. (2012). *Prospección Geoeléctrica en los Alrededores del Volcán de Paipa-Boyacá.* Bogotá: SGC.

González-Idárraga, C., Rodríguez-Rodríguez, G., & Alfaro, C. (2017). *Modelo resistivo del área geotérmica de Paipa a partir de datos Magnetotelúricos.* Bogotá D.C: Servicio Geológico Colombiano.

Haselwimmer, C., Prakash, A., & Holdmann, G. (2013). Quantifying the heat flux and outflow rate of hot springs using airborne thermal imagery: Case study from Pilgrim Hot Springs, Alaska. *Remote Sensing of Environment, 136*, 37-46.

Jaramillo, J., & Rojas, P. (2003). Volcanismo reciente en la Cordillera Oriental de Colombia. *Congreso Colombiano de Geología.* Medellin: Poster.

Jiménez-Muños, J. C., & Sobrino, J. A. (2003). A Generalized Single-Channel Method for Retrieving Land Surface Temperature from Remote Sensing Data. *Journal of Geophysical Research*, 1-9.

Jiménez-Muñoz, J. C., Cristóbal, J., Sobrino, J. A., Sòria, G., Ninyerola, M., & Pons, X. (2009). Revision of the Single-Channel Algorithm for Land Surface Temperature Retrieval From Landsat Thermal-Infrared Data. *IEEE TRANSACTIONS ON GEOSCIENCE AND REMOTE SENSING, 47*, 339-349.

Kuenzer, C., & Dech, S. (2013). *Thermal Infrared Remote Sensing.* Springer.

Llanos Rodríguez, E. M., Bonet, C., & Zengerer, M. (2015). *3D Geological - Geophysical Model Building and Forward and Inverse Modeling of Magnetism and Gravimetry Data from Paipa Geothermal Area, Colombia - Final Report.* Melbourne.

Lund, J., & Boyd, T. (2015). Direct utilization of Geothermal Energy 2015 Worldwide Review. *Proceedings World Geothermal Congress*, 25-29.

Mia, M. B., Nishijima, J., & Fujimitsu, Y. (2014). Exploration and monitoring geothermal activity using Landsat ETM + images A case study at Aso volcanic area in Japan. *Journal of Volcanology and Geothermal Research*, 14-21. doi:10.1016

Moyano, I. (2015). *Modelamiento de Estructuras Geotérmicas Ocultas a partir de la Intepretación de Anomalías Magnetotelúricas de Resistividad en la Región de Paipa, Boyacá-Colombia.* Bogotá: Universidad Nacional de Colombia.

Norini, G., Groppelli, G., Sulpizio, R., Carrasco-Núñez, G., Dávila-Harris, P., Pellicioli, C., . . . De Franco, R. (2015). Structural analysis and thermal remote sensing of the Los Humeros Volcanic Complex: Implications for volcano structure and geothermal exploration. *Journal of Volcanology and Geothermal Research*, 221-237.

Ortiz, I. D., & Alfaro, C. (2010). *Inventario de Puntos de Agua y Geoquímica de las áreas Geotérmicas de Paipa e Iza: Aguas, Suelos y Peloides.* Bogotá: Servicio Geologico Colombiano.

Ren, H., Du, C., Liu, R., Qin, Q., Guangjian, Y., & Li, Z. L. (2015). Atmospheric water vapor retrieval from Landsat 8 thermal infrared images. *American Geophysical Union - Journal of Geophysical Research: Atmospheres*, 1723-1738.

Rodríguez Rodríguez, G. F., & Vallejo Rodríguez, E. F. (2013). *Sondeos Térmicos Superficiales en el Área Geotérmica de Paipa (Boyacá).* Bogotá: Servicio Geológico Colombiano.

Rueda Gutíerrez, J. (2016). *Cartografía de los cuerpos dómicos del área geotérmica de Paipa.* SGC. Bogotá: Servicio Geológico Colombiano.

Sekertekin, A., & Arslan, N. (2019). Monitoring thermal anomaly and radiative heat flux using thermal infrared satellite imagery – A case study at Tuzla geothermal region. *Geothermics*, 243-254. doi:doi.org/10.1016/j.geothermics.2018.12.014

Sobrino, J. A., Jiménez Muñoz, J. C., & Paolini, L. (2004). Land surface temperature retrieval from LANDSAT TM 5. *Remote Sensing of Environment*, 434-440.

Vásquez, L. (2002). *Exploración Geofisica con el Metodo Electromagnetico en el Municipio de Paipa.* Bogotá: SGC.

Vásquez, L. (2012). *Aplicación de Métodos Potenciales en el Área Geotérmica Paipa-Iza.* Bogotá: SGC.

Velandia, F. (2003). *Cartografía Geológica y Estructural Sector Sur del Municipio de Paipa.* Bogotá: SGC.

Wu, W., Zou, L., Shen, X., Lu, S., Su, N., Kong, F., & Dong, Y. (2012). Thermal infrared remote-sensing detection of thermal information associated with faults: A case study in Western Sichuan Basin, China. *Journal of Asian Earth Sciences*, 110-117.

Yu, X., Guo, X., & Wu, Z. (2014). Land Surface Temperature Retrieval from Landsat 8 TIRS—Comparison between Radiative Transfer Equation-Based Method, Split Window Algorithm and Single Channel Method. *Remote Sensing*, 9829-9852.